Fluorescence tomography of targets in a turbid medium using non-negative matrix factorization

Binlin Wu[*] and S. K. Gayen

Physics Department, The City College and the Graduate Center of the City University of New York, 160 Convent Avenue, New York,
New York 10031, USA

A near-infrared optical tomography approach for detection, three-dimensional localization, and cross-section imaging of fluorescent targets in a turbid medium is introduced. The approach uses multisource probing of targets, multidetector acquisition of diffusely transmitted fluorescence signal, and a non-negative matrix factorization based blind source separation scheme to obtain three-dimensional location of the targets. A Fourier transform back-projection algorithm provides an estimate of target cross section. The efficacy of the approach is demonstrated in an experiment involving two laterally separated small fluorescent targets embedded in a human breast tissue-simulating sample of thickness 60 times the transport mean free path. The approach could locate the targets within ~1 mm of their known positions, and provide estimates of their cross sections. The high spatial resolution, fast reconstruction speed, noise tolerance, and ability to detect small targets are indicative of the potential of the approach for detecting and locating fluorescence contrast-enhanced breast tumors in early growth stages, when they are more amenable to treatment.

PACS number(s): 87.85.Pq, 42.25.Dd, 87.63.lt, 87.19.xj

I. INTRODUCTION

The interest in near-infrared (NIR) fluorescence tomography for detection of cancer derives from its superior detection sensitivity and specificity, higher signal-to-background ratio and better spatial resolution than other diffuse optical imaging (DOI) approaches, and potential to provide molecular information on disease-induced changes in biological tissues [1–14]. In addition, advances towards development of target-specific exogenous contrast agents [2,6,15,16], imaging instrumentation [9,17–21], as well as analytical methods and numerical algorithms [3,22–26] hold the promise for noninvasive detection and characterization of tumors in dense tissues, identifying suspect growth as malignant or benign, and assessing the effect of neoadjuvant chemotherapy [27,28]. The key attributes of a clinically useful cancer imaging modality include ability to detect and locate tumors in early stages of growth when those are more amenable to treatment, adequate spatial resolution, speedy image reconstruction, and diagnostic potential. Fluorescence-based approaches are sensitive to molecular changes and may provide useful diagnostic information, but diffuse nature of light propagation in biological tissues impedes spatial resolution.

In this article, we introduce a fluorescence tomography approach that treats detecting and locating targets within a turbid medium (such as tumors inside human breast) as a blind source separation (BSS) problem [29], and seeks a solution based on non-negative matrix factorization (NMF) [30,31]. BSS is a general problem in information theory that involves retrieval of "component" signals from measured signals. The measured signals are weighted mixtures of the component signals contributed by the targets ("blind sources") and may be expressed as

$$X = AS, \qquad (1)$$

where rows of X represent the measured mixed signals, rows of S represent the component signals, and A is the mixing matrix.

NMF is a matrix decomposition method that seeks to factorize matrix X into two non-negative matrices A and S, with the constraint that the contributions of the components and their weights to the measured signal be *non-negative*. It has been extensively used in such diverse applications as facial image recognition [30], genetic and molecular pattern discovery [32], spectral data analysis [33], and cancer class discovery [34]. In this article, we initiate its application to the fluorescence contrast-based DOI problem.

Figure 1 schematically illustrates the measurement scheme of the proposed fluorescence tomography approach for a slab sample that consists of fluorescent targets embedded in a highly scattering turbid medium. The scheme uses multisource illumination of a part of the sample (source plane) by excitation light of wavelength λ_x and multidetector acquisition of the induced fluorescence signals of wavelength λ_m that emerge from the opposite face (detector plane). The excitation light beam incident at a point on the source plane diffusely transits through the sample and induces the embedded targets to fluoresce. Fluorescence from the targets diffusely transits through the sample and gives rise to a two-dimensional (2D) spatial intensity distribution of fluorescence signal on the detector plane, which is recorded by a multiple-detector arrangement. Similar signals are recorded for the excitation beam incident on other points on the source plane. We realize the multisource illumination scheme by step-scanning the sample across the excitation light beam in a two-dimensional (2D) array of grid points, and implement the multidetector signal acquisition scheme by imaging the detector plane onto the sensing element of a charge coupled device (CCD) camera with every pixel acting as a detector. Every recorded fluorescence signal is a weighted mixture of component signals from the fluorescent targets. Such a multisource probing and multidetector signal acquisition culminates in a robust data set for retrieving target information. The task of retrieving target information from these mixtures is a BSS problem and

---

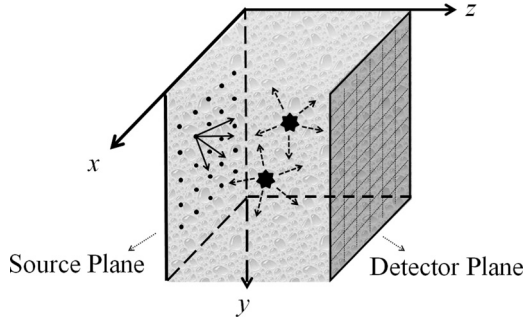[*]Author to whom all correspondence should be addressed: bwu@sci.ccny.cuny.edu

FIG. 1. Multidetector acquisition of fluorescence (wavelength, λ_m) intensity distribution on the detector plane following multisource illumination (wavelength, λ_x) of the source plane of the sample.

here we adapt NMF for the task. The non-negativity constraint makes NMF particularly suited for fluorescence tomography because in principle the fluorescence signal appears on a dark background, and in common practice is measured on a weak background, and hence is expected to be intrinsically positive.

We test the efficacy of the resulting NMF-based fluorescence tomography using experimental data on a "human breast-simulating phantom", that is, a sample whose size and key optical properties are similar to the average values of those parameters for a typical human breast. A useful feature of our experimental arrangement is that simply by removing an optical filter we could use it for absorption contrast-based imaging of the targets to corroborate with fluorescence tomography results. The salient features of this NMF-based fluorescence tomography approach are the following. First, it is considerably less computationally intensive and hence significantly faster than iterative DOI methods that seek to calculate optical properties of every voxel of the sample. Second, it could detect the targets and provide their three-dimensional position coordinates with high accuracy, which is considered to be important for prognosis [35]. Third, the approach is notably noise tolerant. Finally, it could detect rather small targets, which is indicative of its potential for detection of breast tumors in early growth stages when they are more responsive to medical intervention.

The remainder of the article is organized as follows. Section II outlines the theoretical formalism of the NMF-based tomography approach. Section III details the experimental arrangement, materials, and parameters. Section IV presents the results, and Sec. V involves a discussion of the consequences of the results.

II. THEORETICAL FORMALISM

The theoretical formalism for NMF-based fluorescence tomography considers the following problem. The excitation beam of light sequentially illuminates an array of N_s source points on the source plane of the sample realizing multiple-source probing. Once any of these N_s points (excitation sources) is illuminated the diffusely propagating excitation beam of wavelength λ_x induces the targets (fluorescent sources) embedded in the medium to fluoresce. The fluorescence signal at the opposite boundary (detector plane) is recorded by N_d detectors. The formalism considers this

fluorescence signal to be a weighted mixture of signals arriving from the embedded targets. A different signal is obtained when another source point is illuminated. The fluorescence signal measured by the detector at $\boldsymbol{r}_d$ for illumination of the source point at $\boldsymbol{r}_s$ may be expressed as the following form of Eq. (1):

$$x(\boldsymbol{r}_d, \boldsymbol{r}_s) = \sum_j a_j(\boldsymbol{r}_d) s_j(\boldsymbol{r}_s), \tag{2}$$

where $a_j(\boldsymbol{r}_d)$ is the mixing vector, $a_j(\boldsymbol{r}_d)s_j(\boldsymbol{r}_s)$ represents the contribution of the jth target to the signal [7,36], and the sum is over all the targets (fluorescent sources). NMF retrieves $s_j(\boldsymbol{r}_s) = [s_j(\boldsymbol{r}_{s1}), s_j(\boldsymbol{r}_{s2}), \dots, s_j(\boldsymbol{r}_{sN_s})]$ and $a_j(\boldsymbol{r}_d) = [a_j(\boldsymbol{r}_{d1}), a_j(\boldsymbol{r}_{d2}), \dots, a_j(\boldsymbol{r}_{dN_d})]^T$ assuming those to be non-negative, where the superscript T denotes transpose. Commonly used NMF algorithms include the multiplicative update method [30] and alternating least squares (ALS) method [37,38]. We implement the ALS method that uses alternating least squares steps to estimate A (or S), and use that estimate to optimize S (or A), and keep repeating the alternative steps until the desired optimization is obtained. Non-negativity is ensured by setting any negative element of A or S equal to 0. We used an available NMF toolbox [39] to carry out the computation.

Light propagation in a highly scattering medium with embedded fluorescent targets excited by an external light source is approximately described by coupled diffusion equations at the excitation wavelength (λ_x) and emission wavelength (λ_m) [22,24]:

$$-\nabla \cdot [D_x(\boldsymbol{r}, \omega) \nabla \phi_x(\boldsymbol{r}, \omega)] + [\mu_{a_x}(\boldsymbol{r}, \omega) - i\omega/c] \phi_x(\boldsymbol{r}, \omega)$$
$$= \delta(\boldsymbol{r} - \boldsymbol{r}_s), \tag{3}$$

$$-\nabla \cdot [D_m(\boldsymbol{r}, \omega) \nabla \phi_m(\boldsymbol{r}, \omega)] + [\mu_{a_m}(\boldsymbol{r}, \omega) - i\omega/c] \phi_m(\boldsymbol{r}, \omega)$$
$$= \phi_x(\boldsymbol{r}, \omega) \gamma(\boldsymbol{r})/[1 - i\omega\tau(\boldsymbol{r})], \tag{4}$$

where the subscripts x and m denote parameters pertaining to excitation wavelength and emission wavelength, respectively; ω is the modulation angular frequency; $\phi_x(\boldsymbol{r}, \omega)$ and $\phi_m(\boldsymbol{r}, \omega)$ are photon densities at position $\boldsymbol{r}$; μ_{a_x} and μ_{a_m} are absorption coefficients of the medium; $D_x(\boldsymbol{r}, \omega)$ and $D_m(\boldsymbol{r}, \omega)$ are the diffusion coefficients of the medium; $\gamma(\boldsymbol{r}) = \eta \mu_{a_f}(\boldsymbol{r})$ is the fluorescent yield of the fluorophore in the target; and η, μ_{a_f} and $\tau(\boldsymbol{r})$ are the quantum yield, absorption coefficient at the excitation wavelength, and fluorescence lifetime of the fluorophore, respectively.

For localized small fluorescent targets, the fluorescence signal on the detector plane can be expressed as

$$U_m(\boldsymbol{r}_d, \boldsymbol{r}_s, \omega) = \sum_j G_m(\boldsymbol{r}_d, \boldsymbol{r}_j, \omega) f_j(\omega) G_x(\boldsymbol{r}_j, \boldsymbol{r}_s, \omega), \tag{5}$$

where $G_x(\boldsymbol{r}_j, \boldsymbol{r}_s, \omega)$ is a Green's function that describes the propagation of the excitation light of wavelength λ_x from the source at $\boldsymbol{r}_s$ to the jth target contained in volume V_j centered at $\boldsymbol{r}_j$; $G_m(\boldsymbol{r}_d, \boldsymbol{r}_j, \omega)$ is a Green's function that describes the propagation of the fluorescence of wavelength λ_m from the jth target to the detector at $\boldsymbol{r}_d$;

$$f_j(\omega) = \gamma(\boldsymbol{r}_j) c_m V_j/[1 - i\omega\tau(\boldsymbol{r}_j)] \tag{6}$$

is the fluorescence strength of the jth target; and c_m is the speed of light in the medium. Comparing Eqs. (2) and (5) we find

$$s_j(\boldsymbol{r}_s) = \alpha_j G_x(\boldsymbol{r}_j, \boldsymbol{r}_s, \omega), \qquad (7)$$

and

$$a_j(\boldsymbol{r}_d) = \beta_j G_m(\boldsymbol{r}_d, \boldsymbol{r}_j, \omega), \qquad (8)$$

where α_j, β_j are scaling factors. One refers to $s_j(\boldsymbol{r}_s)$ and $a_j(\boldsymbol{r}_d)$ as non-negative component intensity distributions (NCIDs) on the source plane and detector plane, respectively, since those are proportional to the corresponding light intensity distributions and from reciprocity $G_x(\boldsymbol{r}_j, \boldsymbol{r}_s, \omega) = G_x(\boldsymbol{r}_s, \boldsymbol{r}_j, \omega)$. Since we used a slab sample in the experiment, the Green's functions to be used in the above equations are those for slab geometry in the diffusion approximation assuming a uniform background medium, as detailed elsewhere [36,40].

The task of retrieving the locations of the targets involves fitting of the NCIDs to the Green's functions, and we use the following least squares fitting for the jth target:

$$\arg \min_{\alpha_j, \beta_j, \boldsymbol{r}_j} \left\{ \sum_{\boldsymbol{r}_s} \left[\alpha_j^{-1} s_j(\boldsymbol{r}_s) - G_x(\boldsymbol{r}_j, \boldsymbol{r}_s, \omega) \right]^2 \right.$$
$$\left. + \sum_{\boldsymbol{r}_d} \left[\beta_j^{-1} a_j(\boldsymbol{r}_d) - G_m(\boldsymbol{r}_d, \boldsymbol{r}_j, \omega) \right]^2 \right\}. \qquad (9)$$

The fitting using Eq. (9) provides optimal estimates of the two scaling factors α_j and β_j and the location $\boldsymbol{r}_j$ of the jth target. The fluorescence strength then is

$$f_j = \alpha_j \beta_j. \qquad (10)$$

Another important consideration is the size of the targets. A back projection of $U_{m_j}(\boldsymbol{r}_d, \boldsymbol{r}_s, \omega)$ from the detection plane onto the "target plane" ($z = z_j$ plane) provides an estimate of the target size [7]. The fluorescence signal due to the jth target can be approximated by [7]

$$U_{m_j}(\boldsymbol{r}_d, \boldsymbol{r}_s, \omega)$$
$$= \int_{z=z_j} G_m(\boldsymbol{\rho}_d - \boldsymbol{\rho}, \omega) X_j(\boldsymbol{\rho}) G_x(\boldsymbol{\rho} - \boldsymbol{\rho}_s, \omega) d\boldsymbol{\rho}, \quad (11)$$

where $\boldsymbol{\rho}_s$ and $\boldsymbol{\rho}_d$ are the lateral coordinates of the source and the detector, and the integration is over the $z = z_j$ plane. In the Fourier space $X_j(\boldsymbol{q})$ follows from Eq. (11) as

$$X_j(\boldsymbol{q}) = \frac{U_{m_j}(\boldsymbol{q} - \boldsymbol{q}_s, \boldsymbol{q}_s, \omega)}{G_m(\boldsymbol{q} - \boldsymbol{q}_s, \omega) G_x^*(\boldsymbol{q}_s, \omega)}, \qquad (12)$$

where $\boldsymbol{q}$ and $\boldsymbol{q}_s$ are the spatial frequencies on the x-y plane and * denotes complex conjugate. The inverse Fourier transform of $X_j(\boldsymbol{q})$ provides the cross-section image of the jth target at the $z = z_j$ plane.

This NMF-based optical imaging approach may be realized with slab, cylindrical, and other geometries, and with time-resolved, frequency domain, and continuous wave (cw) measurement schemes. Data collected in backscattering mode may be used as well. In this article, we focus on localization of targets with cw ($\omega = 0$) measurements in forward-propagation mode.
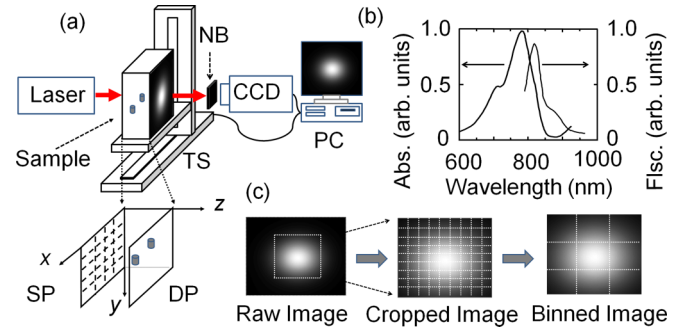

FIG. 2. (Color online) (a) A schematic diagram of the experimental arrangement for imaging objects embedded in a turbid medium. Key: NB = narrow-band-pass filter centered on 830 nm, TS = translational stage, CCD = charge coupled device camera, PC = personal computer, SP = source plane, DP = detector plane. Inset (below) shows the 2D array of points on the source plane that were scanned across the incident laser beam. A typical raw image is shown in the PC monitor. (b) The absorption and fluorescence spectra of ICG in water. (c) A typical raw image (left) detected by the CCD camera is cropped (middle) and binned (right).

III. EXPERIMENTAL MATERIALS AND METHODS

The experimental arrangement used multisource probing and multidetector signal acquisition in forward-propagation geometry, as shown schematically in Fig. 2.

The sample consisted of a 250-mm × 250-mm × 60-mm transparent plastic container filled with Intralipid-20% (Baxter, Product 2B6023) suspension in water as a slab of scattering medium, and two 4.2-mm-diameter × 10-mm cylindrical glass tubes filled with a solution of Indocyanine green (ICG) dye (Sigma-Aldrich, Product I2633) as fluorescent targets. The concentration of Intralipid-20% was adjusted [41] to provide a transport mean free path l_t of ~0.99 mm at $\lambda_x = 790$ nm, and 1.05 mm at $\lambda_m = 830$ nm. We chose the optical properties and the thickness (60 mm) of the sample cell to emulate average values of those parameters for a compressed human breast and the size of the target to resemble that of small tumors. The ICG concentration in the targets was 1 μM which provided an absorption coefficient of 0.027 mm^{-1} at 790 nm, which is closer to the lower end of the concentration range used by other groups and for different *in vivo* applications [3,5,42,43]. The Intralipid-20% concentration in the target was the same as that of the background to ensure that both had the same scattering characteristics. The two targets fluoresced over 790–966 nm with a peak around 825 nm. The targets were placed in the midplane of the sample cell and their known locations appear in Table I. The targets were treated as fluorescent targets for the measurements using emitted light in a narrow band around 830 nm, and as absorptive targets for transillumination measurements using light at the excitation wavelength of 790 nm.

A computerized translation stage (Aerotech Model ATS02015-M-40L with Unidex 511 controller) scanned the sample across a 790-nm, 100-mW, cw diode-laser (Power Technology, Model IQ1C100G2) beam in a two-dimensional (x-y) array of 15 × 11 grid points, with a step size of 5 mm to realize the multisource probing scheme. We refer to the

TABLE I. Known and NMF-retrieved target positions.

Mode	Target	Known positions [x, y, z (mm)]	Retrieved positions [x, y, z (mm)]	Error [Δx, Δy, Δz] (mm)
Fluorescence	Left	14.2, 25.0, 30.0	13.9, 25.8, 30.5	0.3, 0.8, 0.5
	Right	54.2, 25.0, 30.0	55.8, 25.5, 29.2	1.6, 0.5, 0.8
Transmission	Left	14.2, 25.0, 30.0	11.7, 28.0, 31.7	2.5, 3.0, 1.7
	Right	54.2, 25.0, 30.0	55.9, 29.7, 32.2	1.7, 4.7, 2.2

250-mm × 250-mm sample surface that faced the laser beam as the *source plane*, and the opposite face as the *detector plane*. The forward-propagating fluorescence (or, transmitted) signal was collected by imaging the detector plane onto the sensing element of a 1024 × 1024 pixels cooled CCD camera (Photometrics CH350) using a 60-mm focal-length camera lens. Each illuminated 24-μm pixel of the CCD camera served as a detector. For fluorescence imaging, the signal was passed through a narrow-band interference filter centered at 830 nm (FWHM 10 nm, 50% transmission) to effectively block the scattered 790-nm pump light. An interfaced personal computer (PC) controlled the sample scanning, as well as data acquisition and storage operations. The PC recorded the raw images for each scan position, and stored them for subsequent analysis. The same arrangement then acquired another set of images with the narrow-band filter removed. Since the diffusely transmitted 790-nm signal was ~1500 times stronger than the fluorescence signal, we considered this later set of images to be transillumination images, and used those in two different ways. First, analysis of these transillumination images provided an estimate of the average value of $\kappa_x = \sqrt{\mu_{a_x}/D_x}$ for the excitation light. The values of these optical parameters of Intralipid-20% suspension in water happened to be very close for the excitation beam and fluorescence light. Second, the images provided a complementary set of raw data for obtaining information about the targets based on their absorption contrast.

IV. DATA PROCESSING AND ALGORITHM

The acquired data were processed using the following steps.

(i) From each fluorescence image, a region of interest was cropped out and then every 5 × 5 pixels in the cropped image were binned together to 1 pixel to enhance the signal-to-noise ratio.

(ii) The fluorescence data were normalized [3,24,44] using $U/I = \phi_0/I_0$ to remove the contribution of unaccounted factors (such as light-source strength, collection geometry, attenuation in the optical filters and components, etc.), where U and I were the computed and measured fluorescence signals with targets inside the background medium, respectively, and ϕ_0 and I_0 were the computed and measured transmitted signals at the excitation wavelength through the background medium "without" targets inside. As it is not practical to remove the target in real life situations, I_0 was estimated as an average of all images acquired at different scan positions [45]. The data matrix, $X = \{x(\boldsymbol{r}_d, \boldsymbol{r}_s)\}$ was then constructed using the normalized fluorescence signals for all scan positions. One

column of X corresponds to signal accumulated for one scan position.

(iii) NMF decomposition of the data matrix using the ALS algorithm [37,38] was then carried out. The fluorescence signal due to each target and the mixing vector, $s_j(\boldsymbol{r}_s)$ and $a_j(\boldsymbol{r}_d)$, were retrieved, which are NCIDs on the source and detector planes, respectively.

(iv) NCIDs $s_j(\boldsymbol{r}_s)$ and $a_j(\boldsymbol{r}_d)$ were then fitted to the Green's functions, $G_x(\boldsymbol{r}_j, \boldsymbol{r}_s)$ and $G_m(\boldsymbol{r}_d, \boldsymbol{r}_j)$, respectively, using Eq. (9) to find the positions of the targets.

(v) The transmission images were then analyzed using the NMF formalism, treating the targets to be absorptive [31]. As was done for the fluorescence signal, the transmission data were also normalized using $\Delta\phi/\Delta I = \phi_0/I_0$ [24,46,47], where ΔI is the measured perturbation in I_0 due to the presence of targets, and $\Delta\phi$ is the computed perturbation in ϕ_0. Since the targets were more absorptive than the background, $\Delta\phi$ was intrinsically negative, so we used $-\Delta\phi$ for constructing the data matrix to satisfy the non-negativity constraint of NMF [31]. Subsequent steps were similar to those listed above for the fluorescent case.

(vi) The NMF-generated NCIDs from both fluorescence and transmission data were used to calculate the cross-section images of the targets using the back-projection algorithm. Because of the diffuse nature of light propagation in the turbid medium, the estimated cross section is expected to be considerably larger than the actual target size. The calculation of $X_j(\boldsymbol{q})$ using Eq. (12) employed Tikhonov regularization [48], with a modified L-curve method [49] to determine the optimal regularization parameter. However, this optimization is a trade-off between obtaining a closer estimate of target cross section and fewer artifacts in the back-projection image. Since the positions of the targets were obtained from the previous steps, any artifacts cropping up in the back-projection process could be readily identified from their positions. So, instead of using the "corner" of the L curve to find the optimal regularization parameter, we settled for a lower regularization using the criterion that the highest artifact peak reaches ~50% of the target peak to improve the size estimate of the cross-section images. The full width at half maximum (FWHM) of the spatial profile of the cross-section image was used as an estimate of the target size.

V. RESULTS

A. Experimental results

Figures 3(a) and 3(b) show NCIDs of the left target on the detector plane and source plane, respectively. Figures 3(c) and 3(d) present the corresponding spatial profiles along the
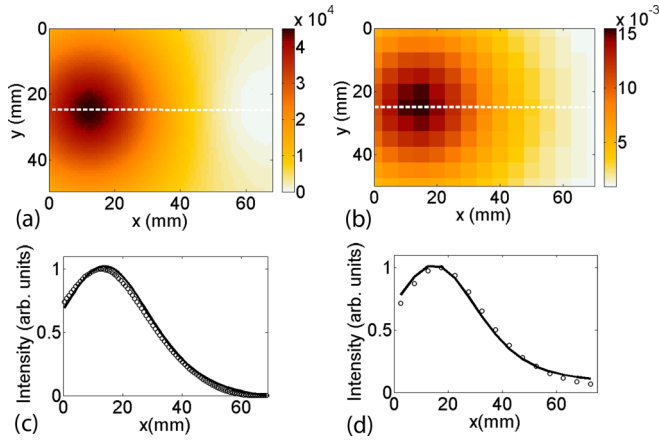
(a) (b) (c) (d)

FIG. 3. (Color online) (a) and (b) NCIDs corresponding to the left target on the detector plane and on the source plane, respectively; (c) and (d) least squares fits to the spatial profiles along the white dashed lines in (a) and (b), respectively.
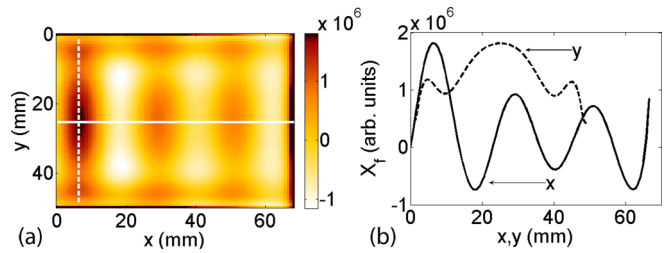

FIG. 4. (Color online) (a) Cross-section image of the left target at the $z = 30.5$ cm plane; (b) corresponding spatial profiles in the x and y directions along the white lines shown in (a).

white dashed lines. The solid curves in Fig. 3(c) and 3(d) are the least squares fits of the experimental profiles, denoted by circles, to the Green's functions using Eq. (9). The resolution of the NCIDs in the detector plane [e.g., Fig. 3(a)] is better than those in the source plane [e.g., Fig. 3(b)], because in our experimental arrangement the signal is collected by a 1024 × 1024 pixels CCD camera, while the source plane is scanned in an x-y array of points, which is much smaller than the number of pixels in the CCD camera.

Table I lists the three-dimensional (3D) locations of the targets extracted from this fitting procedure. Similar NCIDs are obtained for the right target, and the retrieved target positions are also listed in Table I. The retrieved positions agree within ~1 mm of the known positions.

Table I further lists the NMF-retrieved target positions using transillumination data for comparison with those obtained from fluorescence data. There are some small differences in the accuracy of reconstruction of x and y coordinates (that is, in the values of Δx and Δy) for two inclusions. We attribute those to random measurement and/or reconstruction error.

NMF-based fluorescence and transillumination approaches both retrieve locations of the targets well. However, as Table I show, errors in position coordinates of the targets retrieved from fluorescence data are significantly smaller than those obtained from transillumination data. We attribute this difference to the role played by the background in the two cases. Ideally, the fluorescence signal is a measurement of emitted light on a dark background, while the transillumination signal is a perturbation on a strong background. In practice, the background is significantly smaller in fluorescence imaging than in transillumination imaging. Other researchers have reported on similar superior performance of fluorescence tomography as well [3,5]. If the background is substantial (as in the case of fluorescence from the contrast agent uptaken by normal tissue, or tissue autofluorescence) the fluorescence tomography may not retain this edge over the transillumination imaging.

The scaling factors α and β were generated in the least squares fitting using Eq. (9), and the fluorescence strengths were estimated using Eq. (10) to be 11.5 m^3/s and 14.6 m^3/s

for the left and right targets, respectively, while the known value for both targets is 13.4 m^3/s. The uncertainties in the estimated values are 14% and 9% compared to known values. Similarly, the optical absorption strengths $\mu_{a_f}(\boldsymbol{r}_j)c_m V_j$ of the targets were estimated from the transmission data [31] to be 583 m^3/s and 582 m^3/s for the left and right targets, respectively, which were within 20.3% of the known value of 730 m^3/s.

Cross-section images of the targets were generated using the back-projection method. Figure 4(a) displays a pseudo-color cross-section image of the left target at the $z = 30.5$ mm plane generated from the fluorescence data. The real cross-section image of the target is at the left of the frame (confirmed by its location obtained from the previous step), while the other two are artifacts whose strength depends in part on the regularization parameter. A similar cross-section image was obtained for the right target. The full width at half maximum (FWHM) of the spatial profiles of the cross-section images [as in Fig. 4(b) for the left target] were found to be 8.8 and 19.1 mm for the left target, and 8.8 and 18.4 mm for the right target in x and y directions, respectively. The cross-section images estimate the lateral dimensions of the targets to be approximately twice their known values. We presume it a consequence of the diffusive nature of light propagation. However, the ratio between the y and x dimensions of the targets estimated to be 2.2 and 2.1 for the left and right targets, respectively, are close to the actual value of ~2.4 for both targets.

For comparison, similar cross-section images were generated using the transmission data. We found the FWHM to be 7.7 and 18.4 mm for the left target, and 8.4 and 19.1 mm for the right target in x and y directions, respectively. The ratio of the length (y dimension) to the diameter (x dimension) of the targets was estimated to be 2.4 and 2.3 for the left target and the right target, respectively. The cross-section estimates are comparable for both the fluorescence and transillumination approaches.

B. Simulative study of the effect of noise

It is instructive to test the susceptibility of this NMF-based fluorescence tomography approach to noise at this initial phase of development. To assess the effect of noise on retrieving target location, separation between two targets, and optical strength we conducted a simulative study mimicking the experimental conditions. For this purpose, simulated data, i.e., digital images, were first generated using the analytical forward model, Eq. (5). Random Gaussian noise and Poisson

noise were then added to every pixel of every image directly to assess the effect of possible noise that could arise from the fluctuations in laser power, CCD response, dark current, the background fluorescence, and the background room light, etc. The signal intensity at a pixel of the image with this added noise was of the form

$$I'_{ij,k} = I_{ij,k} + f_G I_{ij,k} + f_P < I_{ij,k} > , \qquad (13)$$

where $I'_{ij,k}$ and $I_{ij,k}$ are the signal intensity with and without noise, respectively, at the (i, j)-th pixel of an image recorded when the kth source was illuminating the sample; $f_G I_{ij,k}$ is the multiplicative Gaussian noise with f_G being the fraction of intensity that is added; and $f_P \langle I_{ij,k} \rangle$ is the Poisson noise, with $\langle I_{ij,k} \rangle$ the average of signal intensity over the pixels of all images and f_P the fraction of the average intensity that is added to the pixel. The above equation implies that for 50% multiplicative Gaussian noise, the standard deviation of $f_G I_{ij,k}$ is equal to half of the value of $I_{ij,k}$, i.e., the standard deviation of f_G is 0.5. Similarly, for 50% Poisson noise, the average value of $f_P \langle I_{ij,k} \rangle$ is equal to half of the value of $\langle I_{ij,k} \rangle = (\Sigma_{ijk} I_{ij,k})/(N_s N_x N_y)$, where N_s is the number of source positions, and N_x and N_y are the numbers of pixels in an image in x and y directions. The resultant data set X', each column of which was constructed using the elements of I', was then analyzed using the NMF algorithms. The target properties, background characteristics and other parameters were chosen to be same in this simulative study as those used in the experiment described in Sec. III. The NMF analysis of the noisy image provided NCIDs of both the targets which were then combined to obtain the "recovered image". We explored the reconstruction efficacy of the NMF algorithm for different combinations of multiplicative Gaussian noise and Poisson noise.

Figures 5(a) and 5(b) show raw images of the two 4.2-mm-diameter $\times$ 10-mm cylindrical fluorescent targets on the detector plane generated using the analytical forward model without noise and with noise (50% multiplicative Gaussian noise plus 50% Poisson noise), respectively. The image recovered from Fig. 5(b) using the NMF formalism appears in Fig. 5(c). Even a visual inspection shows that the image quality degrades with the addition of noise [Fig. 5(b)], and that an NMF-based reconstruction of the noisy image improves image quality [Fig. 5(c)]. As a more objective and quantitative metric for image quality we use the peak signal-to-noise ratio (PSNR) defined as [50]

$$\text{PSNR} = 10 \log_{10} \left(\text{MAX}_f^2 / \text{MSE} \right), \qquad (14)$$

where MAX_f is the maximum signal value in the image without noise, and MSE is the mean square error defined as

$$\text{MSE} = \frac{1}{N_x N_y} \sum_{i=1}^{N_x} \sum_{j=1}^{N_y} \| I'_{ij,k} - I_{ij,k} \|^2, \qquad (15)$$

where $I_{ij,k}$ is the image without noise, and $I'_{ij,k}$ is either the noisy image or the NMF-recovered image, corresponding to the kth source.

PSNR for the "noisy image" in Fig. 5(b) is 8.4 while that for the NMF-recovered image is 13.2. We examined the variation of PSNR with noise level keeping multiplicative Gaussian noise fixed at 50% in one case and 20% in another, while varying the Poisson noise. The results, displayed in
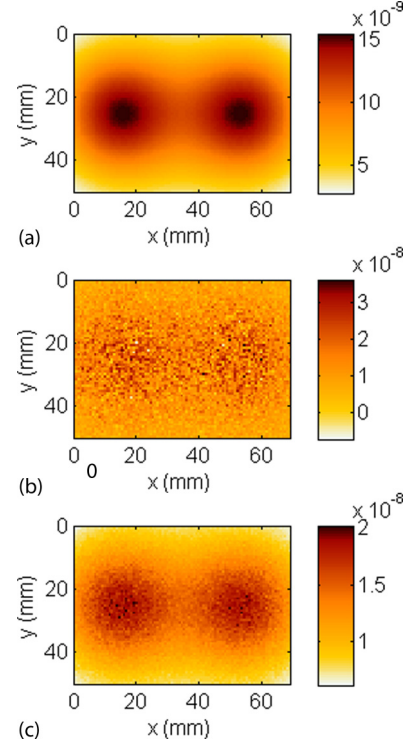

FIG. 5. (Color online) (a) Pseudo-color images generated using analytical forward model without noise. (b) Noisy image generated by adding 50% multiplicative Gaussian noise and 50% Poisson noise. (c) Image recovered using the NMF formalism. Similar images were obtained for other combinations of noise levels.

Fig. 6, show that while the PSNR depends on the overall noise level, the NMF formalism is effective in recovering image from noisy background.

Even for the considerably noisy case of 50% multiplicative Gaussian noise and 50% Poisson noise, NMF formalism retrieved relevant parameters with considerable accuracy. The target locations were retrieved to be exactly the same as the known locations in the zero-noise case and with ~1 mm uncertainty in the lateral direction and <2 mm uncertainty
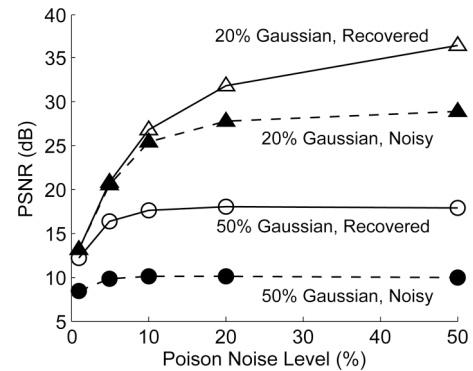

FIG. 6. Variation of PSNR with noise obtained by keeping multiplicative Gaussian noise fixed at a certain level and varying the Poisson noise level, as noted on the curves. The lines connecting the data points represented by circles and triangles are meant for guiding the eyes only.

in the axial direction for the noisy case. The fluorescence strengths were retrieved with ∼0.6% uncertainty for both targets in the zero-noise case, and with ∼9% uncertainty for the noisy case. The size of the targets was estimated to be ∼6 mm in the horizontal direction and ∼27 mm in the vertical direction from the back-projection cross-section images for both zero-noise and noisy cases. The effect of noise seemed to be somewhat pronounced when the targets were brought close together. For center-to-center target separation up to 14 mm (separation between nearest edges ∼10 mm) the target locations were estimated within 1 mm of the known value in all directions for the zero-noise case, while the target locations were estimated within 2 mm in the lateral direction and ∼10 mm in the axial direction for the noisy case.

VI. DISCUSSION

One of the main advantages of NMF-based fluorescence tomography is that it is less computationally intensive and consequently faster than other inverse image reconstruction (IIR) approaches that seek to reconstruct optical properties of every voxel in the sample volume. The reasons are similar to those for absorptive and scattering targets as detailed elsewhere [31]. First, if the sample volume is divided into $N_v = N \times N \times N$ voxels, the number of unknowns in the NMF method is N times less compared to the model-based approaches, which leads to a substantial saving in the computational time when N is large. Second, other IIR methods usually involve iteration of the forward model, while no repeated solution of the forward model is involved in the NMF approach, which makes it faster and computationally less intensive than other IIR approaches. For a typical IIR method [51], the computational complexity is usually $O(N_d N_s N_v^2)$ for a single iteration of the forward model, where N_s, N_d are the numbers of sources and detectors, respectively. When NMF is used, the computational complexity per iteration (intrinsic NMF iteration) is typically on the order of $O(N_d N_s N_k)$ [33], where N_k is the number of components that relates to the number of targets and is usually a small number. Therefore, the computational complexity of the NMF-based approach is much smaller than that for even a single iteration of an iterative IIR method.

While the discussion above provides a theoretical basis for why the NMF-based approach is faster, for a side-by-side comparison, we first tried to use the finite element method (FEM)-based algorithm NIRFAST from the Dartmouth group [52] for the three-dimensional (3D) problem using our experimental data described in Sec. III. Unfortunately, we could not run it on our PC (Intel Core 2 Duo 2.5 GHz CPU and

4GB RAM) because of memory run-out problems! The NMF algorithm could finish the task within 2 min using the same PC. Following the common practice in literature [53,54] we used a two-dimensional (2D) problem which is less computationally intensive than a 3D problem, and made a comparison between the two approaches possible using the above-mentioned PC. The simulation used an 80-mm × 40-mm rectangular sample with $\mu_{ax} = 0.003$ mm^{-1}, $\mu'_{sx} = 1$ mm^{-1}, $\mu_{am} = 0.003$ mm^{-1}, $\mu'_{sm} = 1$ mm^{-1}. Two 5-mm-diameter circular targets with whose $\mu_{af} = 0.1$ mm^{-1}, $\eta = 0.1$, $\tau = 1$ ns were embedded at (20, 20) mm and (60, 20) mm. A 2D finite element mesh was generated using triangular elements whose node-to-node distance is 1 mm. The mesh included 3321 nodes and 6400 elements. Seventeen continuous wave (cw) sources were located on an 80-mm side one l_t (1 mm) below the entrance boundary and evenly distributed with 5-mm spacing between two consecutive sources. Seventeen detectors were placed on the opposite boundary with the same 5-mm spacing between two consecutive detectors. A data set of 17 × 17 source-detector pairs was generated with no intensity modulation. Multiplicative Gaussian noise levels of 20%, 40%, 50%, and 60% were used and compared with 0 noise-level data. A pixel basis of 80 × 40 uniform cells was used for reconstruction.

The target positions were retrieved using both FEM-based and NMF-based approaches, and the results are compared with known locations in Table II. In all cases, the computation time for the FEM-based approach was approximately 2 min each, while NMF-based approach takes less than 2 s on our PC mentioned above. Based on the computational complexity, this difference will be even larger when the size of the mesh increases or/and 3D problems are considered. While at lower noise levels both the approaches retrieved target locations with comparable accuracy, NMF-based approach provided higher accuracy at higher noise levels.

The NMF-based approach is suited for but not limited to small, pointlike targets. Its strength is in detecting small targets, and providing their accurate three-dimensional location, which is of importance for early detection of breast cancer [35]. For extended targets, the retrieved target location is the weighted center of optical strength of the target.

In this initial study to assess the feasibility of NMF-based fluorescence tomography, we focused on the rather idealized situation of negligible background fluorescence. However, in fluorescence imaging of biological tissues background fluorescence is common, and needs to be taken into consideration [3]. Sources of this background include intrinsic fluorescence from

TABLE II. Comparison between FEM- and NMF-based approaches.

Noise (%)	Target positions (x, y) (mm)		
	Known (left target, right target)	FEM retrieved (left target, right target)	NMF retrieved (left target, right target)
0	(20, 20), (60, 20)	(19, 21), (61, 19)	(21.1, 19.9), (58.8, 20.0)
20		(19, 19), (61, 19)	(21.5, 20.9), (58.6, 20.4)
40		(19, 15), (58, 21)	(20.1, 19.6), (57.9, 19.2)
50		(25, 12), (64, 11)	(21.8, 18.8), (59.1, 16.3)
60		(27, 14), (65, 10)	(20.0, 26.7), (59.9, 20.6)
	Computation time	∼120 s	∼2 s

tissue constituents, and fluorescence from exogenous contrast agent that normal tissue adjacent to the tumor may uptake [3,55]. While the contrast agents are designed to preferentially attach to tumors, some uptake by normal tissues is unavoidable, particularly for *in vivo* experiments [3]. However, as has been shown in this article for a transillumination imaging case, NMF can be used in the presence of substantial background. One needs to employ an appropriate background accommodation method and consider fluorescence signal due to targets as perturbation on the background signal [5,31,46,56–58]. In *in vivo* studies, background fluorescence due to contrast agent uptake by normal tissues may be significantly reduced by adjusting the time delay between administration of contrast agent and the measurements, since the contrast agent gets removed from the normal tissue faster than from the tumor [3]. The background due to autofluorescence is minimized using proper choice of excitation wavelength [55].

A simulative study shows that the approach is considerably noise tolerant, providing comparable estimates of the target location, optical strength, and back-projection cross section for 0 noise and 50% multiplicative Gaussian noise plus 50% Poisson noise.

In summary, NMF-based fluorescence tomography can retrieve three-dimensional location of fluorescent targets in a breast phantom rather accurately and provide an estimate of target cross section. It has the potential for detecting and locating contrast-enhanced tumor in a human breast in early stages of growth.

[1] B. P. Joshi and T. D. Wang, Cancers **2**, 1251 (2010).

[2] S. Luo, E. Zhang, Y. Su, T. Cheng, and C. Shi, Biomaterials **32**, 7127 (2011).

[3] A. Corlu, R. Choe, T. Durduran, M. A. Rosen, M. Schweiger, S. R. Arridge, M. D. Schnall, and A. G. Yodh, Opt. Express **15**, 6696 (2007).

[4] I. Gannot, A. Garashi, V. Chernomordik, and A. Gandjbachkhe, Opt. Lett. **29**, 742 (2004).

[5] A. Godavarty, M. J. Eppstein, C. Zhang, S. Theru, A. B. Thompson, M. Gurfinkel, and E. M. Sevick-Muraca, Phys. Med. Biol. **48**, 1701 (2003).

[6] X. He, K. Wang, and Z. Cheng, WIREs Nanomed. Nanobiotechnol. **2**, 349 (2010).

[7] M. Alrubaiee, M. Xu, S. K. Gayen, and R. R. Alfano, Appl. Phys. Lett. **89**, 133902 (2006).

[8] V. Ntziachristos, C. Bremer, and R. Weissleder, Eur. Radiol. **13**, 195 (2003).

[9] V. Ntziachristos, J. Ripoll, and L. V. Wang, Nat. Biotechnol. **23**, 313 (2005).

[10] R. Richards-Kortum and E. Sevick-Muraca, Annu. Rev. Phys. Chem. **47**, 555 (1996).

[11] J. Wu, L. Perelman, R. R. Dasari, and M. S. Feld, Proc. Natl. Acad. Sci. USA **94**, 8783 (1997).

[12] R. Weissleder, C. H. Tung, U. Mahmood, and A. J. Bogdanov, Nat. Biotechnol. **17**, 375 (1999).

[13] S. G. Demos, A. J. Vogel, and A. H. Gandjbakhche, J. Mammary Gland Biol. Neoplasia **11**, 165 (2006).

[14] S. Andersson-Engels, C. Klinteberg, K. Svanberg, and S. Svanberg, Phys. Med. Biol. **42**, 815 (1997).

[15] S. Tyagi, S. A. E. Marras, and F. R. Kramer, Nat. Biotechnol. **18**, 1191 (2000).

[16] H. Lee, W. Akers, K. Bhushan, S. Bloch, G. Sudlow, R. Tang, and S. Achilefu, Bioconjugate Chem. **22**, 777 (2011).

[17] E. M. C. Hillman and A. Moore, Nat. Photonics **1**, 526 (2007).

[18] Y. Chen, X. Intes, and B. Chance, Biomed. Instrum. Technol. **39**, 75 (2005).

[19] N. Ramanujam, J. Chen, K. Gossage, R. Richards-Kortum, and B. Chance, IEEE Trans. Biomed. Eng. **48**, 1034 (2001).

[20] A. T. Kumar, S. B. Raymond, A. K. Dunn, B. J. Bacskai, and D. A. Boas, IEEE Trans. Med. Imaging **27**, 1152 (2008).

[21] F. Leblond, S. C. Davis, P. A. Valdés, and B. W. Pogue, J. Photochem. Photobiol. B. **98**, 77 (2010).

[22] M. S. Patterson and B. W. Pogue, Appl. Opt. **33**, 1963 (1994).

[23] A. D. Klose and A. H. Hielscher, Opt. Lett. **28**, 1019 (2003).

[24] A. B. Milstein, S. Oh, K. J. Webb, C. A. Bouman, Q. Zhang, D. A. Boas, and R. P. Millane, Appl. Opt. **42**, 3081 (2003).

[25] R. Roy, A. Godavarty, and E. M. Sevick-Muraca, IEEE Trans. Med. Imaging **22**, 824 (2003).

[26] Q. Zhu, H. Dehghani, K. M. Tichauer, R. W. Holt, K. Vishwanath, F. Leblond, and B. W. Pogue, Phys. Med. Biol. **56**, 7419 (2011).

[27] S. Jiang, B. W. Pogue, K. E. Michaelsen, M. Jermyn, M. A. Mastanduno, T. E. Frazee, P. A. Kaufman, and K. D. Paulsen, J. Biomed. Opt. **18**, 076011 (2013).

[28] B. J. Tromberg, B. W. Pogue, K. D. Paulsen, A. G. Yodh, D. A. Boas, and A. E. Cerussi, Med. Phys. **35**, 2443 (2008).

[29] J.-F. Cardoso, Proc. IEEE **86**, 2009 (1998).

[30] D. D. Lee and H. S. Seung, Nature **401**, 788 (1999).

[31] B. Wu, M. Alrubaiee, W. Cai, M. Xu, and S. K. Gayen, Int. J. Opt. **2012**, 185435 (2012).

[32] J.-P. Brunet, P. Tamayo, T. R. Golub, and J. P. Mesirov, Proc. Natl. Acad. Sci. USA **101**, 4164 (2004).

[33] V. P. Pauca, J. Piper, and R. J. Plemmons, Linear Algebra Appl. **416**, 29 (2006).

[34] Y. Gao and G. Church, Bioinformatics **21**, 3970 (2005).

[35] N. Kroman, J. Wohlfahrt, H. T. Mouridsen, and M. Melbye, Int. J. Cancer **105**, 542 (2003).

[36] M. Xu, M. Alrubaiee, S. K. Gayen, and R. R. Alfano, Appl. Opt. **44**, 1889 (2005).

[37] P. Paatero, J. Comput. Graph. Stat. **8**, 854 (1999).

[38] P. Paatero and U. Tapper, Environmetrics **5**, 111 (1994).

[39] http://cogsys.imm.dtu.dk/toolbox/nmf/.

[40] M. Lax, V. Narayanamurti, and R. C. Fulton, in *Laser Optics of Condensed Matter*, edited by J. L. Birman, H. Z. Cummins, and A. A. Kaplyanskii (Plenum, New York, 1987), p. 229.

[41] H. J. van Staveren, C. J. M. Moes, J. van Marie, S. A. Prahl, and M. J. C. van Gemert, Appl. Opt. **30**, 4507 (1991).

[42] S. G. Sakka, K. Reinhart, K. Wegscheider, and A. Meier-Hellmann, CHEST **121**, 559 (2002).

[43] M. Sekimoto, M. Fukui, and K. Fujita, Anaesthesia **52**, 1166 (1997).

[44] V. Ntziachristos and R. Weissleder, Opt. Lett. **26**, 893 (2001).

[45] B. Wu, W. Cai, M. Alrubaiee, M. Xu, and S. K. Gayen, Opt. Express **19**, 21956 (2011).

[46] D. S. Kepshire, S. C. Davis, H. Dehghani, K. D. Paulsen, and B. W. Pogue, Appl. Opt. **46**, 1669 (2007).

[47] S. D. Konecky, G. Y. Panasyuk, K. Lee, V. Markel, A. G. Yodh, and J. C. Schotland, Opt. Express **16**, 5048 (2008).

[48] A. N. Tikhonov, Dok. Akad. Nauk SSSR **151**, 501 (1963) [Soviet Math. Dokl. **4**, 1035 (1963)].

[49] P. C. Hansen, SIAM Rev. **34**, 561 (1992).

[50] Q. Hyunh-Thu and M. Ghanbari, Electron. Lett. **44**, 800 (2008).

[51] C. D'Andrea, L. Spinelli, D. Cornelli, G. Valentini, and R. Cubeddu, Phys. Med. Biol. **50**, 2313 (2005).

[52] http://www.dartmouth.edu/~nir/nirfast/.

[53] H. Dehghani, E. E. Matthew, E. Eames, P. K. Yalavarthy, S. Srinivasan, C. M. Carpenter, B. W. Pogue, and K. D. Paulsen, Commun. Numer. Methods Eng. **25**, 711 (2008).

[54] S. R. Arridge, M. Schweiger, M. Hiraoka, and D. T. Delpy, Med. Phys. **20**, 299 (1993).

[55] G. Zacharakis, R. Favicchio, M. Simantiraki, and J. Ripoll, Biomed. Opt. Express **2**, 431 (2011).

[56] J. Lee and E. M. Sevick-Muraca, J. Opt. Soc. Am. A **19**, 759 (2002).

[57] M. A. O'Leary, D. A. Boas, X. D. Li, B. Chance, and A. G. Yodh, Opt. Lett. **21**, 158 (1996).

[58] K. M. Tichauer, R. W. Holt, F. El-Ghussein, S. C. Davis, K. S. Samkoe, J. R. Gunn, F. Leblond, and B. W. Pogue, J. Biomed. Opt. **17**, 066001 (2012).